Fluorophore Selection & Incorporation Contribute to Permeation and Distribution Behaviours of Hyperbranched Polymers in Multi-Cellular Tumour Spheroids & Xenograft Tumour Models

Joshua D. Simpson,[ab] Patrícia F. Monteiro,[c] Gayathri R. Ediriweera,[ab] Amber R. Prior,[ab] Stefan E. Sonderegger,[b] Craig A. Bell,[ab] Nicholas L. Fletcher,[ab] Cameron Alexander,[c] and Kristofer J. Thurecht[ab]*

[a] Centre for Advanced Imaging (CAI), ARC Centre of Excellence in Convergent Bio-Nano Science & Technology (CBNS), ARC Centre for Innovation in Biomedical Imaging Technology (CIBIT), The University of Queensland, Brisbane, QLD, 4072

[b] Australian Institute for Bioengineering & Nanotechnology (AIBN), The University of Queensland, Brisbane, QLD, 4072

[c] School of Pharmacy, University of Nottingham, University Park, Nottingham NG7 2RD, UK.

*k.thurecht@uq.edu.au

KEYWORDS hyperbranched polymers, nanomedicine, fluorescence, multi-cellular tumour spheroid (MCTS) models, xenograft tumour models, bio-nano interactions

Abstract Improving our understanding of how design choices in materials synthesis impact biological outcomes is of critical importance in the development of nanomedicines. Here we show that fluorophore-labelling of polymer nanomedicine candidates significantly alters their transport and cell association in Multi-Cellular Tumour Spheroids (MCTS), and their penetration in breast cancer xenografts, dependent on the type of fluorophore and their positioning within the macromolecular structure. These data show the critical importance of biomaterials structure and architecture in their tissue distribution and intracellular trafficking, which in turn govern their potential therapeutic efficacy. The broader implication of these findings suggests that when developing materials for medical applications, great care should be taken early on in the design process as relatively simple choices may have downstream impacts that could potentially skew preclinical biology data.

Introduction

Polymeric nanomedicines hold the potential to improve prognosis and quality of life in oncology patients.[1] In the preclinical space, it has become commonplace to use biocompatible polymers to imbue chemotherapeutics with favourable pharmacokinetics and biodistribution profiles.[2] The level of control afforded can reduce toxicity and off-target effects commonly associated with traditional chemotherapy.[3] Of the available platforms for the development of nanomedicines for cancer treatment, polymeric materials represent a promising approach owing to their facile synthesis, tailorable nature, modularity, and in many examples, inherent stealth characteristics.

Although polymeric nanomedicines show great promise in preclinical studies, only a handful of materials have met with success in clinical trials.[4,5] Among the commonly cited reasons for stymied clinical translation of polymeric materials is the diverse array of biological interactions

which contribute to unforeseen outcomes.[2] A component of this unpredictability arises from the incomplete characterisation of the underlying physicochemical factors that modulate interactions at the bio-nano interface.[6] Identifying how individual components contribute to holistic biological functionality as well as determining the best means for incorporating desired aspects into polymeric nanomedicines are both critical concepts in developing polymeric materials designed for systemic administration with efficacious delivery.

The importance of materials design for controlling biological outcomes has become a core concept in the current generation nanotechnologies,[7] with numerous examples requiring specific environmental stimuli to be encountered, or other more specific conditions met, in order to ensure efficient and efficacious therapeutic delivery.[8] For instance, through the implementation of degradable linkers[9] or polymers with responsive disassembly[10] or swelling properties.[11] However, it is unclear as to what role selected components used to generate platform may possess on determining whether a colloidal material will encounter its desired release conditions.

An illustrative example of how seemingly minor design choices may have profound impacts concerning biological interactions has been the study of the effect of fluorophore incorporation at a cellular level. Fluorophore selection,[12] loading[13] and positioning[14] have each been identified as important factors that can play an important role in cellular association, uptake and distribution in 2D cell cultures. While these studies cannot directly predict the ultimate *in vivo* behaviour of the materials, the results of such studies do indicate that differences will occur as a result of bio-nano interactions that arise due to subtle changes in material properties.[12,14] As the impact of incorporating dyes has been demonstrated in the application of other systems such as antibody-drug conjugates[15] and peptides,[16] and given the widespread use of fluorescence as a preclinical *in*

vivo imaging modality,[17] the ability of fluorescent labels to alter biodistribution, clearance, and tumour accumulation, is of significance and merits more intensive study.

With numerous material designs available as platforms for developing clinically viable nanomedicines, improving our understanding as to where differences will arise in behaviours exhibited will ultimately be of great utility to improving success during translation.[18,19] Given recent advancement of dendritic material platforms into clinical trials,[20] here we report the behaviours of a polyethylene glycol methacrylate (PEGMA) based hyperbranched polymer (HBP) system labelled with either Rhodamine B (**RhB**) or Cyanine-5 (**Cy5**). Through the exploration of this model system, we aim to provide insight as to how minor differences in macromolecular structure can alter biological interactions, concepts which apply to other small dendritic polymers, and likely other polymeric systems more broadly. We chose to evaluate the systems *in vitro* using a structured 3D co-culture breast cancer spheroid model, and in a breast cancer xenograft model where the distribution and behaviour was evaluated both *in vivo* and in tumour tissue *ex vivo*. Through varying the manner of incorporation, we also explored the role of fluorophore positioning in relation to the described fluorophore-driven impacts

Results and Discussion

Given the expected responses will likely be subtle, we chose a polymer system that has been well established[21–23], and a fundamental materials platform for the fluorophore HBPs which has been characterised for its physical properties in depth elsewhere.[14] For this research, the fluorescent dyes were selected for compatibility with both *in vivo* and *in vitro* fluorescence imaging modalities; i.e. sufficient wavelength to penetrate tissue. They were either incorporated into the PEGMA backbone of the HBPs through the inclusion of a fluorophore-labelled monomer

during polymerisation (**Figure 1a**) or appended to the chain-end through post-synthesis modification (**Figure 1b**), producing either internal (**Int**) or external (**Ext**) variations of the labelled HBPs respectively. As such, dye positioning was controlled either through statistical incorporation into the base architecture, or through subsequent reaction to the remaining amine of the chain end. In order to prevent chain-end interactions that were independent of the fluorophore, PEGMA was added to the remaining chain ends of materials *via* Michael-Addition to ensure differences were on account of the dye and not from other potential factors that may be imparted by end group functionality,[14] for instance, charged or aromatic motifs. Both of these factors have been shown to alter the behaviour of dendritic particles, including hyperbranched polymers previously.[22,24,25]

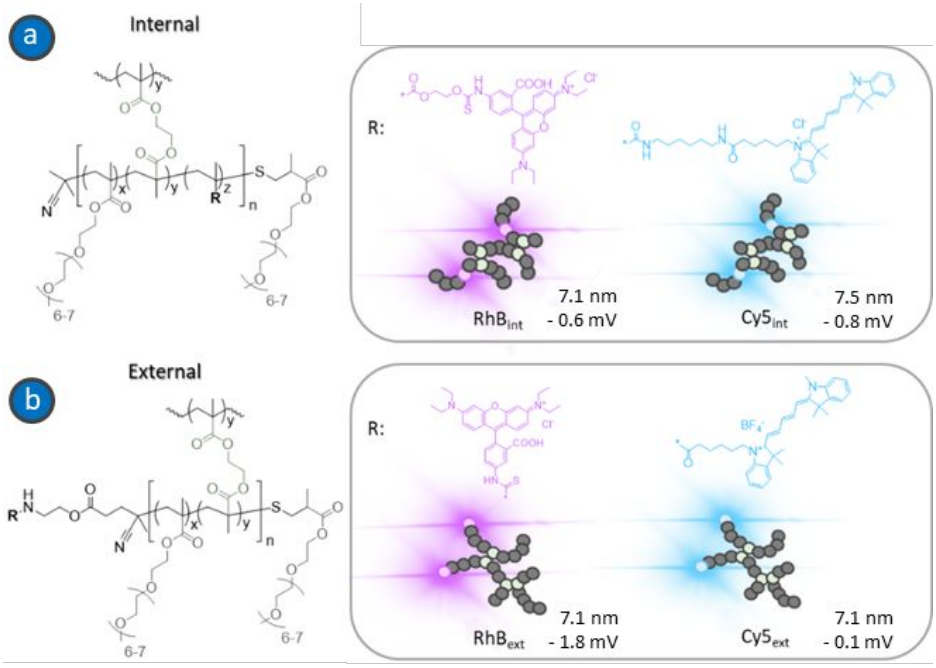

Figure 1: Chemical structures of PEGMA HBPs that differ by fluorophore selection and incorporation. (a) Fluorophore incorporation within the polymer chain structure (left) fluorophore and schematic representation (right). (b) fluorophore introduced to the periphery through post-modification of the chain end, chemical structure (left), fluorophore and schematic

(left). Terms used to refer to the fluorophore incorporation method are labelled on the schematic representations (right). Size and zeta potential are indicated in nm and mV, respectively.

Although the full details of materials synthesis and characterisation are available elsewhere,[14] key factors are summarised in **Table 1**. Of particular pertinence to the results presented in this study, the hyperbranched polymers examined do not differ in terms of labelling efficiency within their pairs, *i.e.* labelling is consistent between **Cy5$_{Int}$** and **Cy5$_{Ext}$** and likewise **RhB$_{Int}$** and **RhB$_{Ext}$**. As such, differences that arise are on account of the dye's positioning within the macromolecular structure and consequent availability, rather than loading efficiency.[14]

Table 1: Summary of fluorophore-HBP characteristics.

	Size (nm)	**Labelling (a.u. per particle)**	**ζ potential (mV)**	**$M_{n,NMR}$ (kDa)**	**$M_{n,SEC}$ (kDa)**	**$Đ_M$**
Unlabelled HBP with BOC-amine	4.5	-	-16.5	10.3	30.3	1.3
Rhodamine B internal HBP	7.1	0.03	-0.6	13.1	51.3	1.48
Rhodamine B external HBP	7.1	0.03	-1.8	-	-	-
Cyanine-5 internal HBP	7.5	0.17	-0.1	13.6	58.7	1.48
Cyanine-5 external HBP	7.1	0.29	-0.8	-	-	-

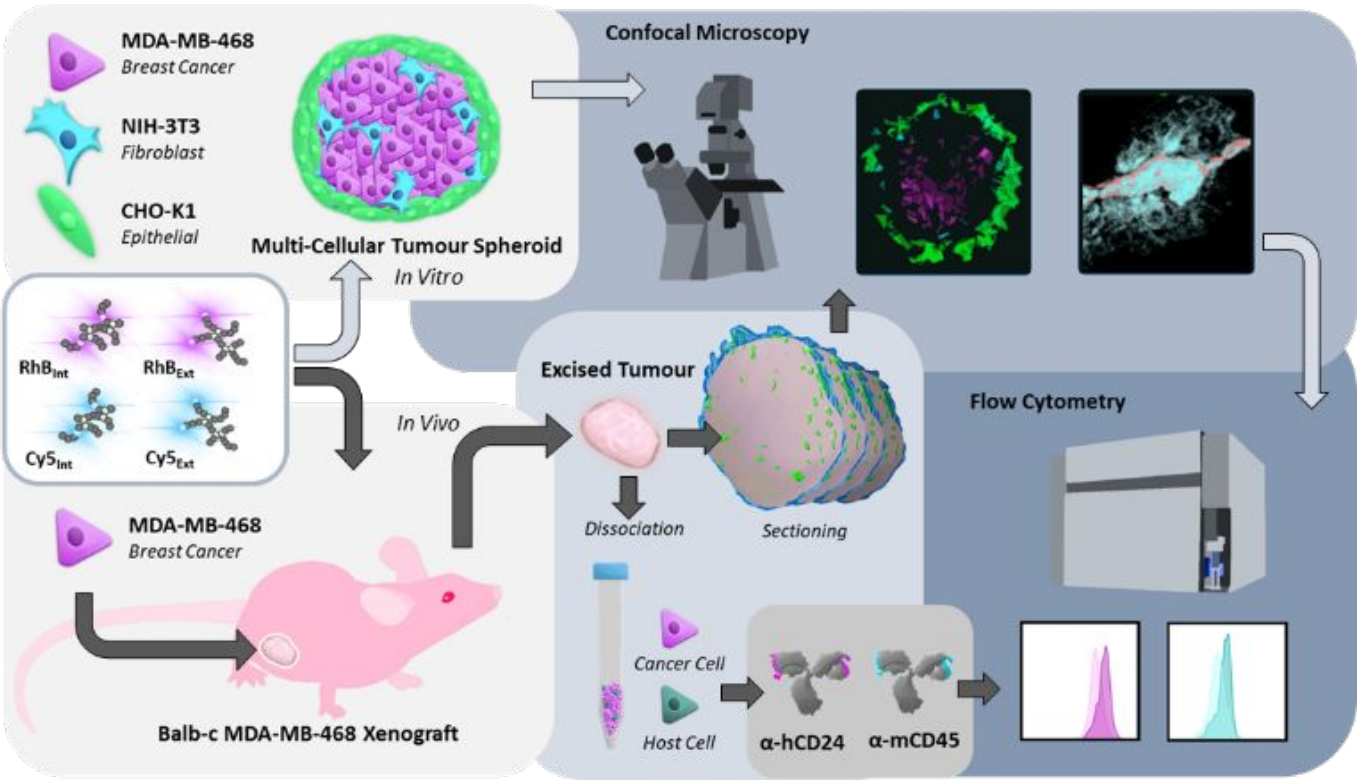

Figure 2: Workflow schematic for assessing permeation of MCTS model and xenograft tumours. MCTS model (top left panel) was exposed to fluorophore-HBPs (middle left panel), examined using confocal microscopy (top right panel) and cell population interactions assessed using flow cytometry (bottom right panel). Tumour interactions were examined using balb-c nu/nu mice with MDA-MB-468 xenograft tumours (bottom left panel), after injection with fluorophore-HBPs (left middle panel) and *in vivo* imaging, tumours were excised, bifurcated and half sectioned (middle panel top right) for confocal microscopy (top right panel) while the cell populations from the other half were harvested (middle panel lower left), labelled based on species origin (middle inset panel) and assessed for polymer fluorescence using flow cytometry (bottom right panel).

To explore the biological impacts of the fluorophore, we elected to utilise an MDA-MB-468 breast cancer model for the selected xenograft, as we have previously demonstrated that the cell line used to establish tumours is susceptible to dye-mediated effects.[14] It has been reported that breast cancer cells exhibit changes in gene expression and efflux mechanisms[26] when grown in 3D

culture, which may influence the fluorophore-driven distributions previously reported in 2D assays,[12,14] we examined the influence of fluorophore in a co-culture model. The 3D co-culture was designed with the aim to recapitulate the more complex *in vivo* environment; specifically, the region first encountered after extravasation, the tumour stroma (**Figure 1** top panel). Building on existing techniques,[26] we established a multi-cellular tumour spheroid (MCTS) model based on low adhesion 3D co-culture of fibroblast (NIH 3T3), breast cancer (MDA-MB-468) and epithelial (CHO-K1) cells. In order to produce a structured model that could potentially replicate some of the characteristics of a xenograft tumour, the 3T3 and MDA-MB-468 cells were used to form a mosaic core spheroid, and CHO-K1 provided an outer epithelial layer. Rodent epithelial and fibroblast cells were selected to recapitulate aspects of the xenograft tumour, and the human cancer cell line was also used to establish tumours in murine models (**Figure 2** bottom left). The structural composition and morphology of the model was verified through confocal microscopy, with individually CellTrace CFSE labelled populations of each cell line imaged within the MCTS (**Figure 3a**).

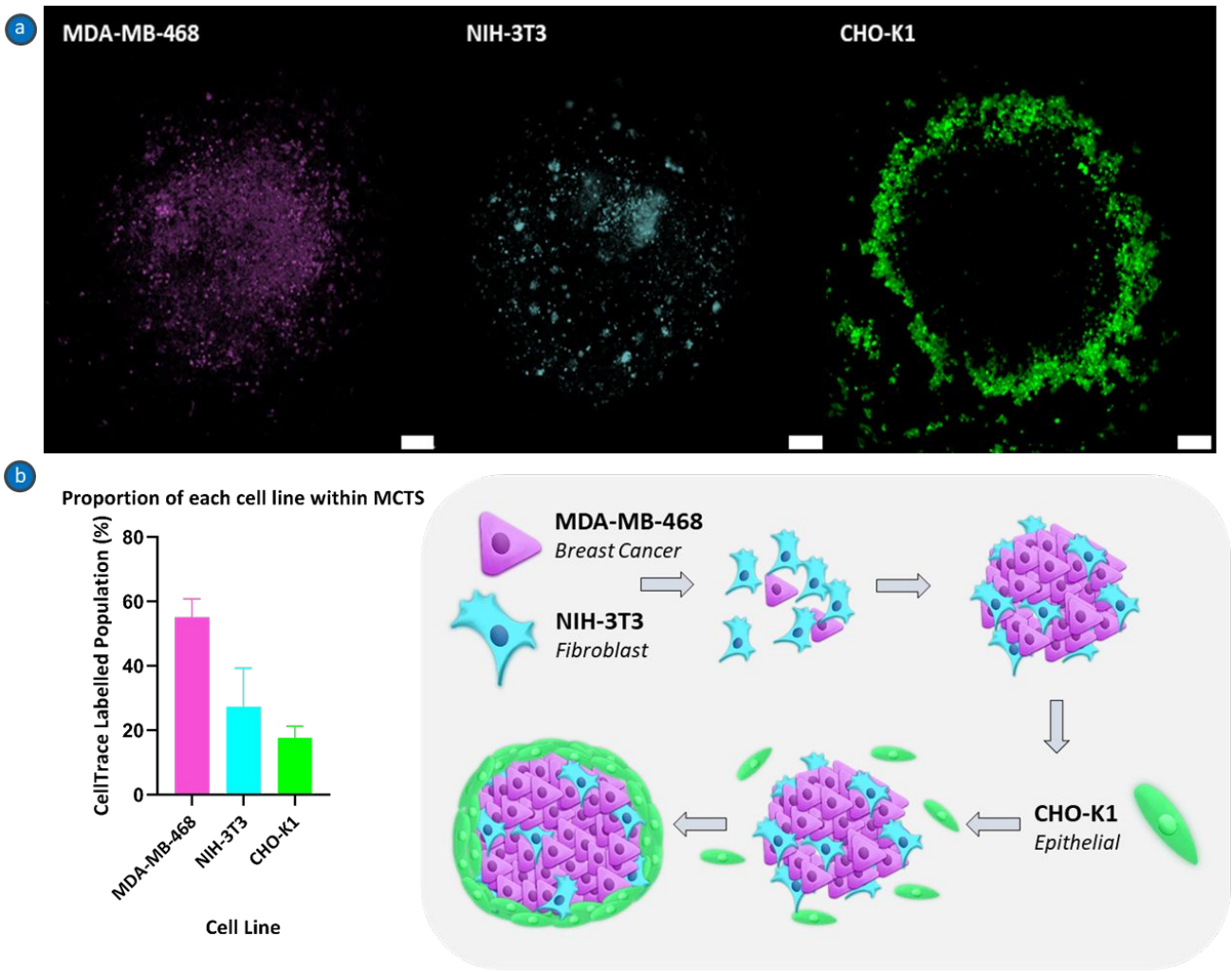

Figure 3: Development of the structured MCTS model. Consisting of three cell lines, each MCTS possessed a distinct structure **(a)** with MDA-MB-468 breast cancer cells forming the core (magenta), NIH-3T3 fibroblasts pushed towards the proliferative zone (cyan), and CHO-K1 epithelial cells forming an outer layer (green), as assessed by flow cytometry **(b)** MDA-MB-468 forming the bulk of the spheroid, with NIH 3T3 fibroblasts and CHO-K1 epithelial cells contributing approximately a quarter of the total population each. Schematic summary of spheroid formation (bottom left panel).

The composition of each cell-type that comprised the MCTS model was further assessed using flow cytometry (**Figure 3b**). The MDA-MB-468 cells formed the bulk of the MCTS (55 ± 6% of

the spheroid), whereas the NIH-3T3 and CHO-K1 populations contributed approximately a quarter of the total population (27 ± 12% and 18 ± 4% respectively). Distribution of each fluorophore-HBP derivative was then examined in permutations of these cell components of MCTS, with each cell population labelled with CellTrace CSFE for analysis after 4 h incubation (**Figure 4a**). When MCTSs were exposed to fluorophore-HBPs, differences between derivatives that varied by the ***positioning*** of the fluorophore were stark, whereas, no significant difference was observed on account of the dye selected. This may be due to both dyes having been identified as being able to enhance cellular interaction to a large extent on account of their lipophilicity,[12,14] however their impact is diminished when made less accessible through placement within the hydrophilic core of the polymer.[14]

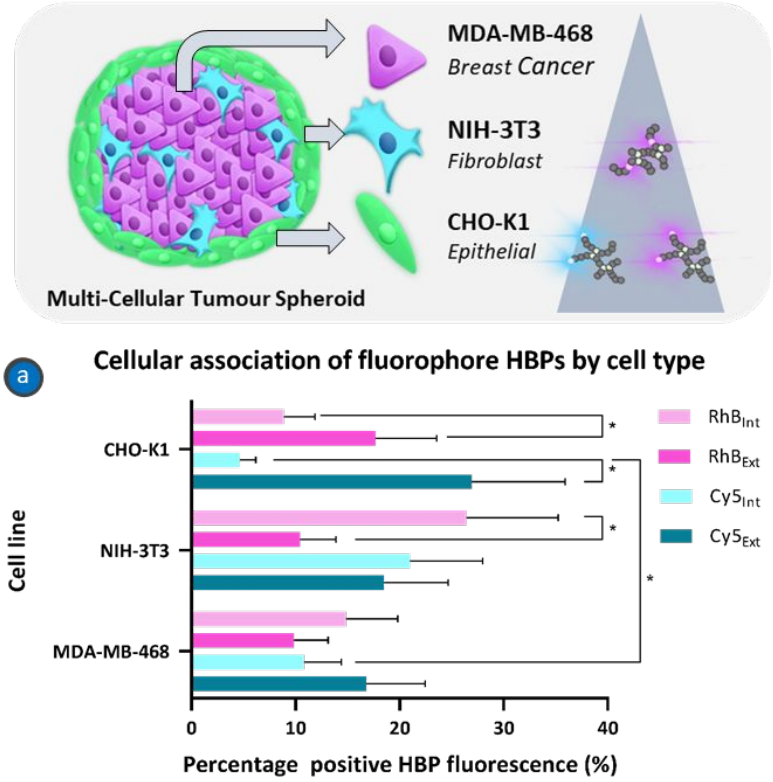

Figure 4: Association of fluorophore-HBPs with cell populations in MCTS model. Schematic structure of the spheroid model linking population association to permeation of the mass and diagrammatic summary of the key results (top panel). **(a)** Bar graph of the percentage of cell

population positive for fluorophore-HBPs; Rhodamine B (magenta) internal (light) and external (dark), Cyanine-5 (cyan) internal (light) and external (dark).

In both Cy5 and RhB samples, internal derivatives showed increased association with fibroblasts when compared to the epithelial layer. In particular, **$Cy5_{Int}$** was present in < 8% of the CHO-K1 cells, being significantly lower than in the other cell populations. **RhB_{Int}** showed a strong preference for the NIH-3T3 cells, being much higher than **RhB_{Ext}** in the same population. Conversely, $fluorophore_{Ext}$ HBPs showed no direct affinity for any specific cell type, showing no statistically significant association to any particular component of the MCTS; however, both displayed significantly increased association with the cells of the epithelial layer when compared to the corresponding HBPs with fluorophore contained within the polymer chain. This is likely due to the non-specific nature of the lipophilic-driven interaction, and that these epithelial cells were the first cells encountered during incubation. Of particular note, no significant difference was observed for interaction between any of the fluorophore-HBPs and the breast cancer cells of the mosaic core. The lack of difference in the MDA-MB-468 cells is surprising, given reports of a negative correlation between membrane affinity and spheroid penetration of peptides.[27] Our prior observations in 2D culture also indicated $fluorophore_{Ext}$ HBPs have improved membrane association.[14] However, the improved association with the peripheral layer of epithelial cells indicates that this effect may just be related to the statistical potential that each cell type is encountered during permeation. The ability of the fluorophore to impact the penetration of the HBPs likely being tied to the membrane characteristics of each cell line,[28] in addition to being encountered sequentially.

These results in a tumour stroma mimicking MCTS model suggest that depending on the impacts of prior biological interactions and barriers (e.g. protein fouling in serum), both external

derivatives possess improved interactions with the cell lines selected to reflect host cell populations at the tumour site, i.e., epithelial cells and fibroblasts, when compared to their internal analogues. Having identified fluorophore-HBP dependent differences in the MCTS model, we sought to compare the behaviours of these materials in xenograft models, through both *in vivo* biodistribution and *ex vivo* tumour tissue distribution studies.

MDA-MB-468 tumour bearing Balb/c nude mice were imaged at 4 and 24 h after injection of fluorophore-HBPs. Example images of each polymer distribution at 24 h are shown in **Figure 5a** (cohort images for Rhodamine-B and Cyanine-5 are available in **Figures S1**, and **S2** respectively). At 4 h post-injection, qualitative differences arose, with signs of bladder clearance in mice exposed to **Cy5$_{Ext}$** and indication of fluorescence in the gastrointestinal tract for those injected with **RhB$_{Ext}$** and **RhB$_{Int}$** (**Figure S3**). At 24 h post-injection (**Figure 5a**), the fluorescence arising from the Rhodamine B label was visibly lower within the tumour mass compared to surrounding tissue, with **RhB$_{Ext}$** exhibiting a slight increase in comparison to **RhB$_{Int}$** (**Figure 5a i-ii**, highlighted with box, fluorescence only inset). **Cy5$_{Int}$** behaved as per prior observations of control HBPs within our team,[9,21,29] with only dim fluorescence at the tumour site (**Figure 5a iii**). In stark contrast, **Cy5$_{Ext}$** exhibited improved tumour fluorescence; however, the images for both Cyanine-5 derivatives may have benefitted from improved signal to noise ratio and depth of penetration due to being a near-infrared dye, compared to the Rhodamine B polymers.

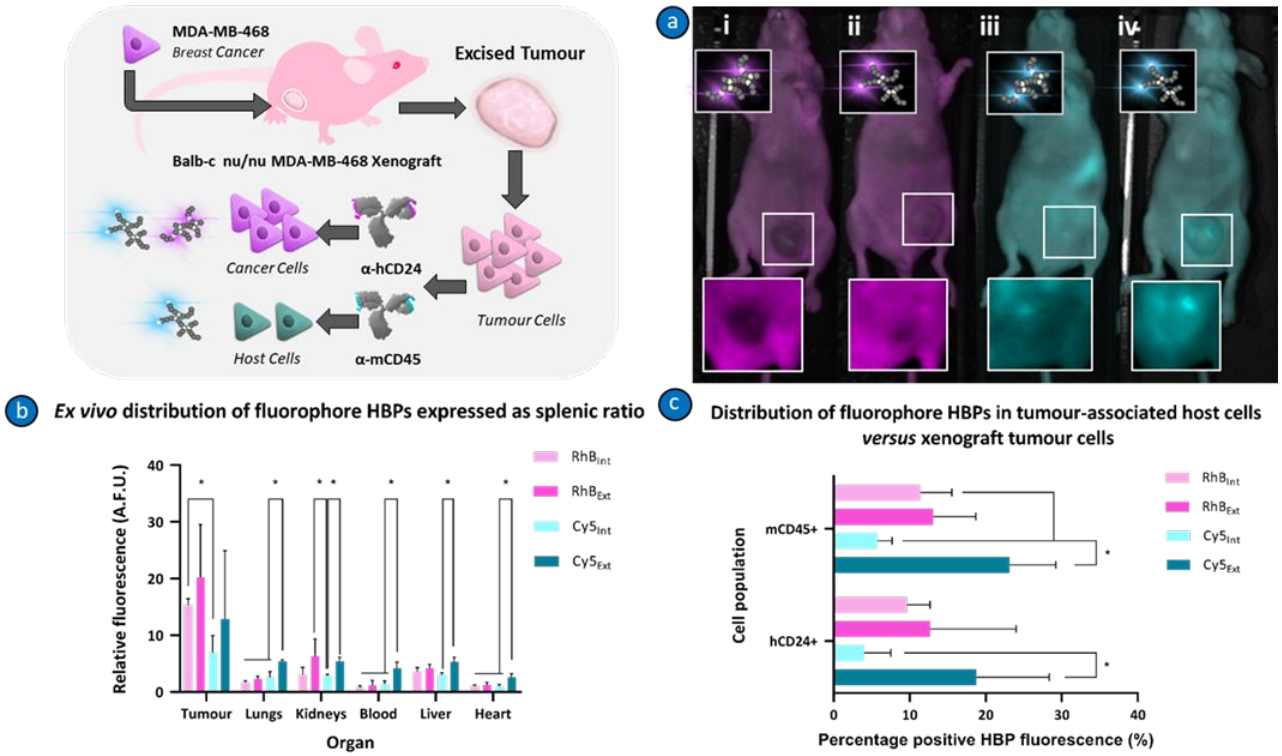

Figure 5: *In vivo* and *ex vivo* biodistribution of fluorophore-HBPs. Schematic of the experimental workflow. **(a)** Example *in vivo* fluorescence images overlaid on mouse photograph, showing the distribution of **RhB_{Int} (i), RhB_{Ext} (ii) $Cy5_{Int}$ (iii)** and **$Cy5_{Ext}$ (iv)**; fluorescence only tumour images provided for clarity **(inset). (b)** Fluorophore-HBP organ distribution assessed *ex vivo* (normalised to spleen; Rhodamine B (magenta), internal (light) and external (dark), Cyanine-5 (cyan), internal (light) and external (dark). Association of fluorophore-HBPs with tumour (hCD24+) and host (mCD45+) cells, shown as percentage positive **(c)**: Rhodamine B (magenta) internal (light) and external (dark) and Cyanine-5 (cyan) internal (light) and external (dark).

To better interpret the distribution of our fluorophore-HBPs, mice were sacrificed, and the fluorescence of the organs and tumour was assessed ratiometrically to facilitate more insightful comparison between fluorophores (**5b**). This normalisation allows for discrepancies due to quenching effects to be accounted for without the need for individual correction factors. When the fluorescence signal is expressed as a ratio to the spleen in all organs, only **$Cy5_{Int}$** displayed

significantly less fluorescence in the excised tumour, in comparison to its Rhodamine B labelled counterpart, suggesting that while positioning imparts a more significant effect *in vivo*, the selected component still plays a role in tumour accumulation. Both external HBP derivatives exhibited higher fluorescence in the kidneys than **$Cy5_{Int}$**. However, there was no significant difference between the Rhodamine B variants, suggesting that in **RhB_{Ext}** the effect of position yields less renal clearance than does **$Cy5_{Ext}$**. No statistical difference between the Rhodamine B derivatives and **$Cy5_{Int}$** within the liver implies that fluorophore selection does not drive excretion through this pathway, although in the case of Cy5, positioning can potentially impact accumulation. The heightened fluorescence arising from **$Cy5_{Ext}$** in the lungs and blood suggests that this particular HBP may possess unique bio-nano interactions systemically.

Beyond these interactions, the only significant differences between the fluorophore-HBPs in the organs assessed *ex vivo* (**Figure S4**), were that **$Cy5_{Int}$** demonstrated less accumulation in the liver than **RhB_{Int}** and overall **$Cy5_{Ext}$** possessed higher fluorescence than **$Cy5_{Int}$** in the examined organs except within the tumour. These results could represent either heightened non-specific entry into tissues and cells, i.e. association with vascular endothelium, or a longer biological half-life, with the signal from the blood enhancing organ fluorescence. The former hypothesis matches the observed CHO-K1 affinity of the MCTS model (**Figure 4a**). Overall, the biodistribution data suggest that the internal derivatives may possess favourable properties in terms of organ *versus* tumour accumulation. Further, these results imply that it may be possible to utilise **RhB_{Int}** as a means of subtly improving uptake of materials at the tumour site without drastically impacting biodistribution, reflecting the improved association demonstrated in NIH-3T3 cells of the MCTS model when compared to the CHO-K1 epithelial layer.

To better understand how the fluorophore-HBPs were behaving at the tumour site, interactions with the xenografted human cancer cells and host tumour-associated populations were analysed through flow cytometry. Tumours were dissociated, and the resulting cell populations fluorescently labelled using antibodies for mouse CD45+ (mCD45+, to label common cancer-associated cell populations from the host) and human CD24+ (hCD24+ to detect human tumour cells), cells positive for either marker being assessed for their fluorophore-HBP fluorescence (**Figure 5c**). Unlike in the MCTS observations, no significant difference in association was detected between $\mathbf{RhB_{int/ext}}$ and the cell origins, whereas conversely, the $\mathbf{Cy5_{Ext}}$ exhibited only qualitatively improved association with both human and mouse cells when compared to $\mathbf{Cy5_{Int}}$. Further, $\mathbf{Cy5_{Ext}}$ also demonstrated a higher affinity for host cells than $\mathbf{RhB_{Int}}$, supporting the notion that the higher $\mathbf{Cy5_{Ext}}$ *ex vivo* fluorescence may be on account of increased translocation into CD45+ vascular endothelial cells.

As the final stage of our assessment of these HBPs across physiological scales, we analysed tumour tissue *ex vivo* to ascertain if fluorophores or their positioning pose any influence over extravasation or subsequent permeation of the tumour mass by our HBPs.

In both the external derivatives, interactions with the tumour stroma were apparent. Collected images indicated enhanced interactions of $\mathbf{Cy5_{Ext}}$ **(Figure 6a iv**) with the stromal barrier in comparison to $\mathbf{Cy5_{Int}}$ (**Figure 6a ii**); however, an appreciable signal was present within the tumour tissue. Further, for $\mathbf{Cy5_{Ext}}$ blood vessels were clearly labelled in the Cy5 channel (**Figure S5**), indicating that this derivative possesses increased interaction with the tumour vasculature. Interestingly, the Rhodamine B derivatives did not ubiquitously label blood vessels (**Figure 6a i-ii**), many of the Dylight stained vessels did not possess notable Rhodamine B fluorescence. In

many of the samples, aggregates of polymer positive for vascular stain were observed outside of vessels, particularly towards the tumour periphery, matching prior reporting.[30]

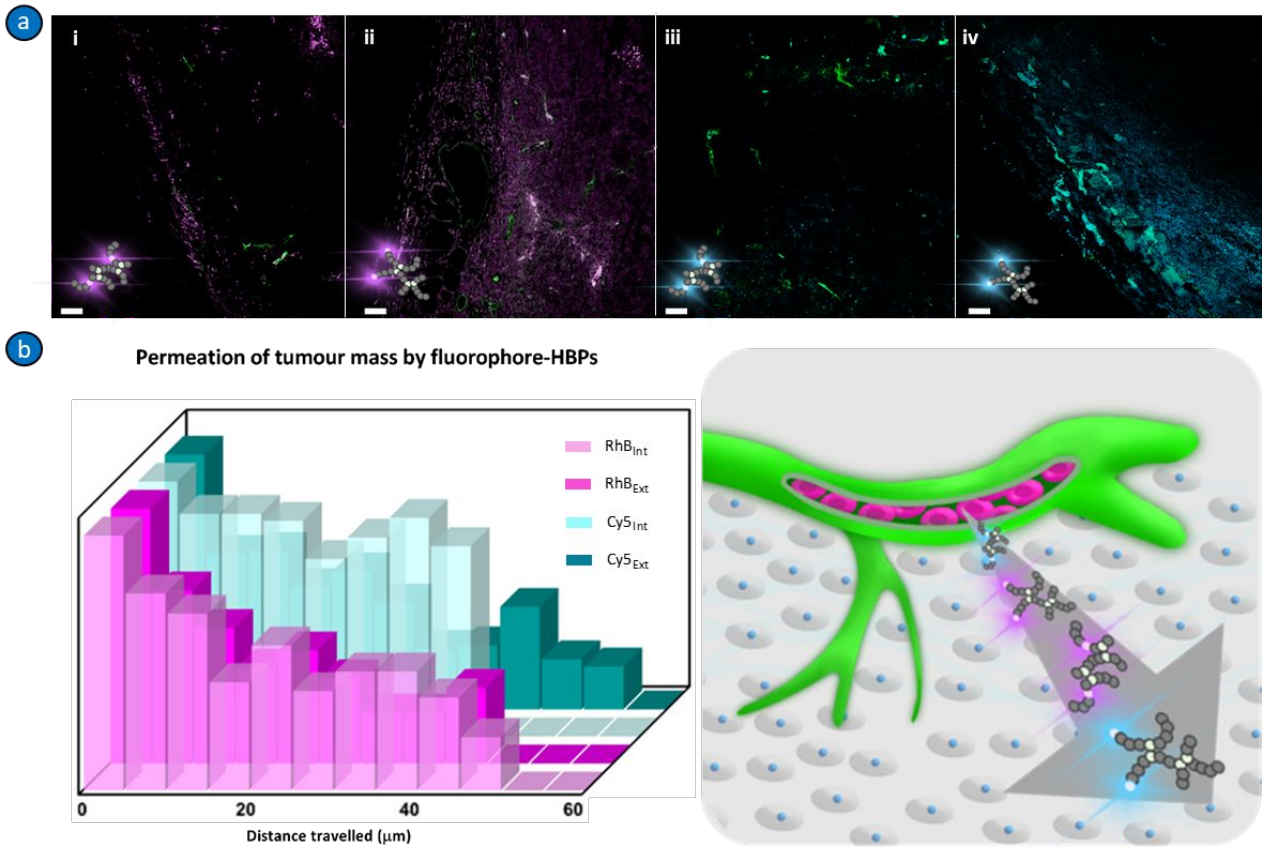

Figure 6: Permeation of tumours by fluorophore HBPs assessed using *ex vivo* confocal microscopy. (a) Confocal micrographs of *ex vivo* tumour slices from mice exposed to Rhodamine B internal **(i)** external **(ii)** and Cyanine-5 internal **(iii)** and external **(iv)**, Rhodamine (magenta), Cyanine-5 (cyan), Dylight labelled blood vessels (green), scale bars represent 100 μm. **(b)** Representation of natural log transform data (see **Figure S6**), showing fluorescence intensity as a function of distance from highest intensity vasculature pixel. **Bottom right: Schematic summary of *ex vivo* tumour permeation data.** Rhodamine B labelled HBPs (**RhB$_{Int}$ and RhB$_{Ext}$**) behaving similarly in terms of permeating the tumour mass, whereas **Cy5$_{Int}$** demonstrated the shortest average transit of all fluorophore HBPs, and **Cy5$_{Ext}$** exhibited the furthest, indicating that

fluorophore selection and placement possess differing impacts throughout biological transit. Schematic summary of the permeation data (bottom right panel).

With the exception of **$Cy5_{Int}$**, the distribution of the fluorescence signal of the HBPs away from blood vessels exhibits an exponential decay (**Figure S6; Tables S1** & **S2**). Due to the complexity of transport, this information is simply a descriptor of bulk distribution away from the vasculature and is not a direct measurement of diffusion. Through the application of a natural log transform of the signal obtained from the line of response data, end of transit is better highlighted (**Figure 6b**). Using this approach, the differences in the distance travelled from the vasculature toward the centre of the tumour mass were distinguishable in a more discrete fashion. The average of each series yielded a defined and unique cut off, distinctly indicating the end of transit (**Figure 6b**) which was influenced by both dye selection and positioning of the fluorophore for each polymer. **RhB_{Int}** and **RhB_{Ext}** showed similarities in terms of distance travelled, whereas Cy5 variations were distinctly dissimilar. All fluorophore-HBPs were generally observed within 60 μm of blood vessels; however, **$Cy5_{Int}$** was on average < 40 μm from adjacent vessels but showed the best permeation of the tumour mass to this distance. This data is supported by co-localisation analysis of the tumour slice images (**Figure S7**) yielding similar data in the form of R^2 values, with a higher rate of pixels containing both fluorophore and vascular stain fluorescence in samples wherein the HBP is has permeated more (**Figure 7**).

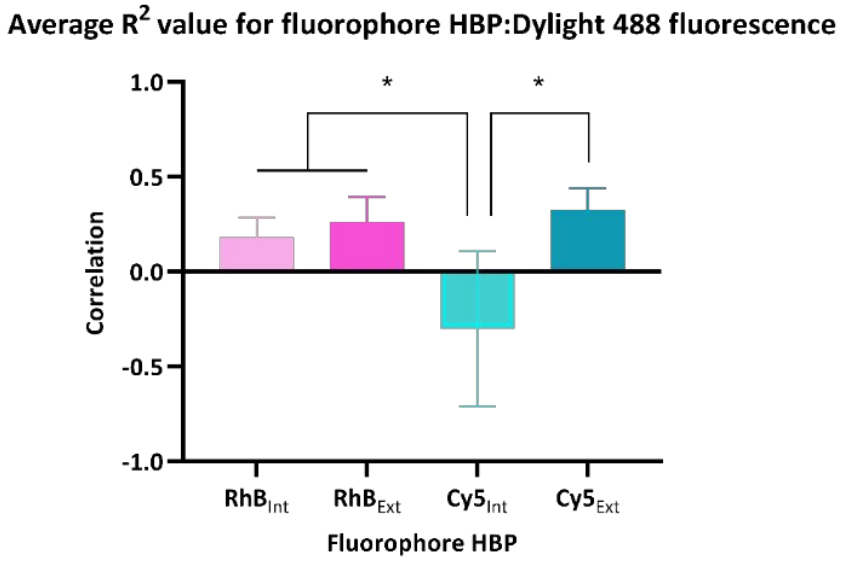

Figure 7: Co-localisation of fluorophore HBP fluorescence with Dylight labelled blood vessels. All fluorophore HBPs showed a low degree of co-localisation with tumour vasculature, indicating an interaction with the endothelial barrier, with the exception of **$Cy5_{Int}$** which exhibited no statistical correlation. These results indicate that **$Cy5_{Int}$** may possess a distinct biological interaction at the tumour site.

These data match the degree of interaction with the epithelial layer of the MCTS model, indicating that the non-specific interactions may enhance extravasation and transit to an extent; however, they are also associated with increased interactions with tumour-associated cell populations. This indicates that the impact of the observations described may be enhanced in tumours with larger proportions of associated cell types such as fibroblasts and macrophages. Further, as the models examined are based on a singular cell line, the roles of heterogeneity and tumour density have not been explored, which likely hold the potential to exaggerate or lessen the behaviours described. This is especially pertinent when considering that when different cell lines are chosen to establish xenograft models, each will yield tumours with different densities, host cell

populations, tumour stroma, vascular architecture, and packing densities. The impact of appending fluorophores to the chain-end may have more exaggerated effects in tumour models with greater production of stroma, for instance, desmoplastic orthotopic pancreatic models.[31,32] As such, the role of fluorophore selection and positioning will most likely require tailored characterisation to each system to which a material is administered. It is essential to consider the impacts of component selection and incorporation in regards to smaller particles such as HBPs, dendrimers, and peptide conjugates, as well as the behaviour of breakdown products in terms of clearance and downstream impacts of larger architectures, *e.g.* micelles, polymersomes, and polymer-coated liposomes.

Conclusions

The impacts of fluorophore selection and positioning have the potential to alter the outcomes of bio-nano interactions across physiological scales. The probe and the manner of its incorporation both contribute to the ability of hyperbranched polymers to penetrate MCTS models, imparting better membrane permeation when placed towards the periphery of the hydrophilic corona. Further, these factors in materials design exhibited differences in biodistribution, clearance pathways, tumour accumulation, extravasation and tumour permeability. Our results also support the use of more complex biological models, such as the structured MCTS used here, as they offer much more predictive power when speculating across physiological scales, and confirm their utility as part of the preclinical pipeline between 2D assays and *in vivo* experiments.

The impact of fluorophore selection and positioning across physiological scales highlights the need for careful deliberation in the design and preclinical assessment of materials. The fluorophores used in this study possess far less impact upon the physicochemical properties of the

polymeric material than do many other imaging probes and other common post-modification moieties. These findings suggest that common practices, such as changing probes for specific applications or assessment of incomplete materials, could lead to incorrect assumptions regarding the behaviour of the material in biological contexts. Once more of these impacts have been identified, it is possible that through rational and holistic design, selection of components could synergistically improve the overall performance and functionality of prospective nanomedicines.

Methods

Synthesis, purification & characterisation of fluorophore-HBPs

The synthesis of the HBPs used in this research has been described in depth with full characterisation available elsewhere.[14] In brief, the materials were synthesised using reversible addition-fragmentation chain transfer (RAFT) polymerisation. Utilising PEGMA to establish the polymer backbone and EGDMA to produce branching, the chain transfer agent leaving a tert-butyl protected amine as the R-group of the chain end for external derivatives. In the case of $\mathbf{Cy5_{Int}}$ and $\mathbf{RhB_{Int}}$ the reaction mixture contained pre-labelled fluorescent monomers. After deprotection of the amine, $\mathbf{Cy5_{Ext}}$ and $\mathbf{RhB_{Ext}}$ were produced via fluorophore species being reacted to the R group of the chain end through a standard isothiocyanate reaction. For consistency, the ester bond connecting the fluorophore to the chain end matches that of the fluorophore to the pre-labelled monomers. The RAFT end group (Z) was removed for both variants through aminolysis and Michael-Addition of PEGMA. HBPs were purified through dialysis and SEC purification. These polymers were characterised using ^{1}H-NMR, UV-Vis, and SEC.

All NMR experiments were undertaken on either a Bruker Avance 500 MHz high-resolution NMR spectrometer. Diffusion weighted spectra (DOSY) were collected at a gradient strength (gpz6) of 15% for a minimum of 128 scans. Chemical shifts are reported as δ in parts per million

(ppm) and referenced to the chemical shift of the residual solvent resonances ($CDCl_3$ ^1H: $\delta = 7.26$ ppm). The resonance multiplicities are described as s (singlet), d (doublet), t (triplet), q (quartet), m (multiplet) or br (broad).

Particle sizing was determined from the diffusion coefficient of the HBPs in D_2O using diffusion ordered spectroscopy (DOSY). Fifty milligrams of HBP was dissolved in 600 μL of D_2O, then a series of 16 spectra were collected at 256 scans each using a linear gradient ramp from 2–85% of the maximum gradient strength. A gradient duration (d) of 3 ms and diffusion time (D) of 250 ms was used in all cases, and all results were calibrated to the diffusion coefficient of D_2O ($D = 2.299 \times 10^{-9}$ m^2 s^{-1}). The Stokes–Einstein equation was then used to calculate the hydrodynamic diameter (D_h).

Size exclusion chromatography (SEC) was performed on a SEC-MALLS chromatographic system consisted of a 1515 isocratic pump (Waters), a 717 autosampler (Waters), Styragel HT 6E and Styragel HT 3 columns (Waters), 2414 differential refractive index detector (Waters) and a Dawn Heleos laser light scattering detector (Wyatt). THF was used as the mobile phase with a flow rate of 1 mL min^{-1}. dn/dc values were calculated using a refractometer and calculated to be 0.069 L g^{-1} for the HBPs.

Zeta potential was achieved using a Zetasizer Nano ZS (Malvern Instruments) at 25 °C and was determined using a high concentration folded capillary zeta potential cell. All HBP samples were solubilised to a concentration of 5 mg mL^{-1} in H_2O. Laser Doppler Velocimetry was used to determine electrophoretic mobility, which was used to determine zeta potential from the Smoluchowski equation.

UV-Vis measurements were performed on a Nanodrop 2000C spectrophotometer (Thermo Scientific) using a low volume (700 μL) quartz cuvette with a 10 mm path length. Absorbance maxima were recorded at 557 and 647 nm for RhB and Cy5 absorbances respectively.

Cell culture & maintenance

To produce the multi-cellular tumour spheroid (MCTS) model as a simplified version of the tumour stroma, we utilised cell lines to represent populations of breast cancer cells (MDA-MB-468), fibroblasts (NIH-3T3), and healthy epithelial cells (CHO-K1). The MDA-MB-468 cells were the same as those used to establish the xenograft tumours, and the fibroblast and CHO-K1 cells were selected to represent the rodent cell populations associated with the tumour. These cell lines were grown in Dulbecco's Modified Eagle Medium (DMEM) (Sigma-Aldrich) supplemented with 10% foetal bovine serum, penicillin, streptomycin and glutamine. These cells were incubated at 37 °C with 5% CO_2 in a water-jacketed incubator, being passaged through mechanical shearing as required. All experiments were performed between passages 10-20.

Production of the MCTS model

In order to produce spheroids with the desired structural features, a mosaic core of cancer and fibroblast cells was generated as per the low adhesion centrifugation methodology outlined by Monteiro et al. (2020)[26] with the epithelial layer attached as an additional step using a protocol modified to mimic Corning Technical Note CLS-AN-390.[33] To utilise this method of spheroid formation, cells were incubated in low adhesion round bottom 48 well plates (Corning). The core formed through co-culture of MDA-MB-468 and NIH-3T3 cells in a ratio of 1:3, the spheroids were required to be large to better reflect penetration issues *in vivo*; thus this amounted to 1000:3000 cells from both cell lines per well respectively. Once plated, the entire plate was centrifuged at 200g for 3 min. The plate was placed in the incubator and left for 3 days. After this

time, 2000 CHO-K1 cells were added to each well, and the plate returned to the incubator for 6 h to allow free cells to settle on the spheroid or bottom of the well, the plate was then centrifuged at 100g for 5 min to encourage attachment to the bottom of the mosaic core, and the plate returned to the incubator overnight.

Verification of structural features of the MCTS model

To ensure that the MCTS yielded the correct structural formation that would separate it from a standard co-culture spheroid, variations of the model were produced with individual cell populations labelled with CellTrace CFSE (Sigma-Aldrich). Cells being labelled as per supplier protocol, with n = 4 of each MCTS generated. At the end of the establishment process, spheroids were imaged in the well plate using a Zeiss 710 confocal microscope. This microscope is housed within the Australian Nanofabrication Facility Queensland node (ANFF-Q) and is equipped with helium-neon, argon, and 405 diode lasers, an incubation chamber, 10x, 20x and 40x W objectives. The MCSTs were imaged at 37 °C using a modified FITC imaging set up (detection range was set to 498-598 nm). Proportionality of these MCTSs was assessed by exchanging the media for phosphate-buffer saline, breaking apart the MCTS, pipetting the solution to ensure equal distribution of the cells, and flow cytometry performed using a Cytoflex flow cytometer (Beckman Coulter). Data were analysed using FlowJo (BD) with live cells being gated through forward and side scatter to remove autofluorescent dead cells, and assessed for FITC fluorescence.

Association of Fluorophore-HBPs with cell populations in MCTSs

In order to examine whether the fluorophore-HBPs had unique interactions with any of the cell layers, MCSTs were produced with CellTrace CFSE labelled populations of MDA-MB-468, NIH-3T3, or CHO-K1, with n = 12 of each produced for comparison. The MCTSs were exposed to 100 μg mL^{-1} of the desired fluorophore-HBP and returned to the incubator for 4 h. Fluorophore-HBP

media was gently removed from the wells, and each MCTS washed three times with PBS containing 10% FBS, to ensure that interactions did not occur during preparation of the samples for flow cytometry. The MCTSs were then broken apart using a pipette tip, centrifuged and resuspended in PBS containing 10% FBS. These cell solutions were then assessed for both CellTrace and fluorophore-HBP fluorescence using a Cytoflex flow cytometer (Beckman Coulter). Data were analysed using FlowJo (BD), initial gating was performed to select for live cells and then fluorescence was analysed using the quadrant gating tool, to identify double-positive populations (both cell trace and fluorophore-HBP). Data were analysed in Excel and exported to Graphpad Prism (Graphpad Software) for graphing.

Establishment of xenograft model

MDA-MB-468 cells were grown en masse and cells harvested and suspended in phosphate-buffered saline for injection to produce the breast cancer xenograft model. Determined using the resource equation method, 18 Female Balb-c nu/nu mice were obtained from the Animal Resource Centre (Western Australia, Australia) at 8 weeks of age. Orthotopic xenograft tumours were induced after anaesthetising the mice using isoflurane by injection of MDA-MB-468 cells (27G, 50 uL) into the mammary fat pad, with each mouse receiving 1 x 106 cells per injection. The mice were returned to their enclosures and tended as per ethical requirements. Four mice were assigned to each fluorophore-HBP group, and two were to receive saline injections.

Biodistribution of fluorophore-HBPs *in vivo* & *ex vivo*

At 12 weeks after inoculation, tumours were palpable, and the mice were seen to be otherwise healthy and randomly allocated to imaging cohorts. Mice were anaesthetised and injected with 100 µl of a 5 mg mL^{-1} solution of the assigned fluorophore-HBP, or 100 µl of isotonic saline solution in the case of control mice. At 4 and 24 h post-injection, mice were anaesthetised, an ophthalmic

ointment was applied, and the mice imaged in their cohorts in both supine and prone positions, being imaged using an IVIS *in vivo* imaging system (Perkin Elmer) using preset protocols for Rhodamine and Cyanine-5. After imaging at the 24 h time point, all mice were injected with Dylight 488 (Sigma-Aldrich) to label vasculature and sacrificed while still under anaesthesia via cervical dislocation. The mice were dissected, the tumours excised and organs were harvested immediately. The organs and tumours were placed into Petri dishes and imaged using the prior settings. After imaging, the tumours from each mouse were bifurcated, one half being fixed overnight in paraformaldehyde, the other being passed through a cell strainer (Sigma-Aldrich), with the latter yielding solutions in 2 mM EDTA, which were kept on ice for transport and immediately taken for assessment using flow cytometry. In the analysis of the organs, mean fluorescence intensity was taken from each organ, the data being exported to Excel for analysis. The fluorescence data were normalised to account for the different quantum yields of the dyes and presented as a ratio of the splenic value. Data was exported to Graphpad Prism (Graphpad Software) for the production of graphs.

Association of fluorophore-HBPs with tumour and host cells

The cell solutions resulting from cell straining were placed in a 96 well plate, centrifuged at 300 RCF for 10 min and labelled using antibodies for human CD24 and mouse CD45 (1/2000 dilution); the plate was then left on ice for 1 h in the dark, before the addition of PBS containing EDTA and 2% FBS. The plate was spun again at 300 RCF for 10 min, the pellets resuspended and taken for measurement. In order to produce populations for gating and compensation, samples were produced from control tumours. Cellular association of fluorophores and antibodies was assessed using an LSRFortessa X-20 flow cytometer (BD). Data were analysed using FlowJo (BD) to examine positive populations for hCD24 or mCD45, and the fluorescence of these cell populations

assessed for fluorophore-HBP fluorescence. Data were analysed in Excel and exported to Graphpad Prism (Graphpad Software) for graphing.

Confocal imaging of tumour blood vessels *ex vivo*

After being fixed overnight, the tumour halves were embedded in paraffin, sectioned using a microtome and dewaxed through xylene washes before hydration using decreasing ratios of ethanol/water solutions. Slides were then sealed using coverslips and clear nail polish. These samples were then imaged using the Zeiss 710 described previously, with a sequential scan utilised to improve the spectral separation of the 488 nm excited Dylight from the Rhodamine B derivative polymers (excited using the 561 nm laser line). Images were taken at 0.6x zoom to show overall behaviour within the tumour slice, and higher zoom applied for imaging of individual blood vessels. Data were analysed in Excel and exported to Graphpad Prism (Graphpad Software) for model fitting, analysis and graphing. For co-localisation analysis, images were exported from Zen Zeiss Lite (Zeiss GmbH) as raw TIFF files, imported into ImageJ, and assessed using the co-localisation tool, scatterplots and co-localisation maps being exported as images, data to Excel for analysis, before graphing in Graphpad Prism. Representative data for demonstrating transit distance was plotted in excel.

Statistical analysis and assessment of fluorophore-HBP transit distance & attrition

To improve upon qualitative assessment of the distance that each fluorophore-HBP travelled from the vasculature, lines of response (LoR) were drawn from the centre of each vessel towards the tumour centre (n = 10 measurements for each HBP across tumours from 3 mice). Each LoR was drawn longer than needed, with data being recorded from the highest intensity value from the Dylight channel, indicating the vascular boundary. Values were collected within 60 μm from the highest Dylight intensity value. The lines were normalised to detect their highest and lowest

intensity points, the average of these lines was then compared to a single exponential decay, and the data graphed as a natural log transform to highlight the average cut-off wherein the average value retrieved is too low to be considered continuous transit.

ASSOCIATED CONTENT

Supporting Information: additional in vivo & ex vivo images & data, additional confocal images of ex vivo tumour slices, additional information for natural log transform of lines of response data, and co-localisation data for ex vivo tumour slices

AUTHOR INFORMATION

Corresponding Author

*Professor Kristofer J. Thurecht

k.thurecht@uq.edu.au

Centre for Advanced Imaging (CAI), ARC Centre of Excellence in Bio-Nano Convergent Science & Technology (CBNS), ARC Centre for Innovation in Biomedical Imaging Technology (CIBIT), The University of Queensland, Brisbane, QLD, 4072

Australian Institute for Bioengineering & Nanotechnology (AIBN), The University of Queensland, Brisbane, QLD, 4072

Present Addresses

Joshua D. Simpson

Centre for Advanced Imaging (CAI), ARC Centre of Excellence in Bio-Nano Convergent Science & Technology (CBNS), ARC Centre for Innovation in Biomedical Imaging Technology (CIBIT), The University of Queensland, Brisbane, QLD, 4072

Australian Institute for Bioengineering & Nanotechnology (AIBN), The University of Queensland, Brisbane, QLD, 4072

Patrícia F. Monteiro

School of Pharmacy, University of Nottingham, University Park, Nottingham NG7 2RD, UK

Gayathri R. Ediriweera

Centre for Advanced Imaging (CAI), ARC Centre of Excellence in Bio-Nano Convergent Science & Technology (CBNS), ARC Centre for Innovation in Biomedical Imaging Technology (CIBIT), The University of Queensland, Brisbane, QLD, 4072

Australian Institute for Bioengineering & Nanotechnology (AIBN), The University of Queensland, Brisbane, QLD, 4072

Amber R. Prior

Centre for Advanced Imaging (CAI), ARC Centre of Excellence in Bio-Nano Convergent Science & Technology (CBNS), ARC Centre for Innovation in Biomedical Imaging Technology (CIBIT), The University of Queensland, Brisbane, QLD, 4072

Australian Institute for Bioengineering & Nanotechnology (AIBN), The University of Queensland, Brisbane, QLD, 4072

Stefan E. Sonderegger

Australian Institute for Bioengineering & Nanotechnology (AIBN), The University of Queensland, Brisbane, QLD, 4072

Craig A. Bell

Centre for Advanced Imaging (CAI), ARC Centre of Excellence in Bio-Nano Convergent Science & Technology (CBNS), ARC Centre for Innovation in Biomedical Imaging Technology (CIBIT), The University of Queensland, Brisbane, QLD, 4072

Australian Institute for Bioengineering & Nanotechnology (AIBN), The University of Queensland, Brisbane, QLD, 4072

Nicholas L. Fletcher

Centre for Advanced Imaging (CAI), ARC Centre of Excellence in Bio-Nano Convergent Science & Technology (CBNS), ARC Centre for Innovation in Biomedical Imaging Technology (CIBIT), The University of Queensland, Brisbane, QLD, 4072

Australian Institute for Bioengineering & Nanotechnology (AIBN), The University of Queensland, Brisbane, QLD, 4072

Cameron Alexander

School of Pharmacy, University of Nottingham, University Park, Nottingham NG7 2RD, UK

Kristofer J. Thurecht

Centre for Advanced Imaging (CAI), ARC Centre of Excellence in Bio-Nano Convergent Science & Technology (CBNS), ARC Centre for Innovation in Biomedical Imaging Technology (CIBIT), The University of Queensland, Brisbane, QLD, 4072

Australian Institute for Bioengineering & Nanotechnology (AIBN), The University of Queensland, Brisbane, QLD, 4072

Author Contributions

The manuscript was written through contributions of all authors. All authors have given approval to the final version of the manuscript.

Funding Sources

National Health and Medical Research Council (KJT; APP1148582), Australian Research Council (LP180100486, CE140100036, IC170100035), Engineering and Physical Sciences Research Council (Grant Nos. EP/N006615/1, EP/N03371X/1 and EP/H005625/1), and the Royal Society (CA; Wolfson Research Merit Award WM150086).

Notes

The authors declare no competing financial interests. All animal experiments were approved by the University of Queensland Animal Ethics Committee and followed the Australian Code of Practice for Use of Animals for Scientific Purposes (AIBN/142/19/UQ).

ACKNOWLEDGMENT

The authors would like to acknowledge the National Health and Medical Research Council for fellowship support (KJT; APP1148582) and the Australian Research Council (LP180100486). This work was supported by the Engineering and Physical Sciences Research Council (Grant Nos. EP/N006615/1, EP/N03371X/1 and EP/H005625/1), and funding by the Royal Society (CA; Wolfson Research Merit Award WM150086) is acknowledged. The research program was funded through the ARC Centre of Excellence in Convergent Bio-Nano Science and Technology (CE140100036) and in part by the ARC Training Centre for Innovation in Biomedical Imaging Technologies (IC170100035). This work was performed in part at the Australian Nanofabrication Facility Queensland node (ANFF-Q) and University of Queensland's School of Biomedical

Science (SBMS). The authors would like to thank Dr. Zachary H. Houston and Dr. Dewan T. Akhter for help with *ex vivo* dissections.

ABBREVIATIONS

2D two-dimensional, 3D three-dimensional, CD24 Cluster of Differentiation 24, CD45 Cluster of Differentiation 45, Cy5 Cyanine-5, Ext external fluorophore, $Đ_M$ Dispersity, DMEM Dulbecco's Modified Eagle Medium, EDTA Ethylenediaminetetraacetic acid, FBS Foetal Bovine Serum, FITC Fluorescein isothiocyanate, HBP Hyperbranched Polymer, Int Internal fluorophore, kDa kiloDalton, LoR Line of Response, MCTS Multi-Cellular Tumour Spheroid, mL millilitre, mg milligram, mV millivolts, $M_{n,NMR}$ Number average Molecular weight by NMR, $M_{n,SEC}$ Number average Molecular weight by SEC, nm nanometer, NMR Nuclear Magnetic Resonance, PBS phosphate-buffered saline, PEGMA polyethylene glycol methacrylate, RAFT reversible addition-fragmentation chain transfer, RhB Rhodamine B, SEC Size Exclusion Chromatography, µg microgram, µm micrometre

REFERENCES

1 Balasubramanian V., Liu Z., Hirvonen J. and Santos H., Nanomedicine: Bridging the Knowledge of Different Worlds to Understand the Big Picture of Cancer Nanomedicines, *Adv. Healthcare Mater.*, 2018, **7**, 1–23.

2 Simpson J., Smith S., Thurecht K. and Such G., Engineered Polymeric Materials for Biological Applications: Overcoming Challenges of the Bio–Nano Interface, *Polymers (Basel).*, 2019, **11**, 1441.

3 Cagel M., Grotz E., Bernabeu E., Moretton M. and Chiappetta D., Doxorubicin: Nanotechnological Overviews from Bench to Bedside, *Drug Discovery Today*, 2017, **22**, 270–281.

4 Bobo D., Robinson K., Islam J., Thurecht K. and Corrie S., Nanoparticle-Based Medicines: A Review of FDA-Approved Materials and Clinical Trials to Date, *Pharm. Res.*, 2016, **33**, 2373–2387.

5 Sun Q., Zhou Z., Qiu N. and Shen Y., Rational Design of Cancer Nanomedicine: Nanoproperty Integration and Synchronization, *Adv. Mater.*, 2017, **29**, 1606628.

6 Wai L., Ho C., Liu Y., Han R., Bai Q., Hang C. and Choi J., Nano-Cell Interactions of Non-Cationic Bionanomaterials, *Acc. Chem. Res.*, 2019, **52**, 1519–1530.

7 El-Sawy H., Al-Abd A., Ahmed T., El-Say K. and Torchilin V., Stimuli-Responsive Nano-Architecture Drug-Delivery Systems to Solid Tumor Micromilieu: Past, Present, and Future Perspectives, *ACS Nano*, 2018, **12**, 10636–10664.

8 Fletcher N., Kempe K. and Thurecht K., Next-Generation Polymeric Nanomedicines for Oncology: Perspectives and Future Directions, *Macromol. Rapid Commun.*, 2020, **2000319**, 1–10.

9 Zhao Y., Houston Z., Simpson J., Chen L., Fletcher N., Fuchs A., Blakey I. and Thurecht K., Using Peptide Aptamer Targeted Polymers as a Model Nanomedicine for Investigating Drug Distribution in Cancer Nanotheranostics, *Mol. Pharmaceutics*, 2017, **14**, 3539–3549.

10 Wong A., Mann S., Czuba E., Sahut A., Liu H., Suekama T., Bickerton T., Johnston A. and Such G., Self-Assembling Dual Component Nanoparticles with Endosomal Escape Capability, *Soft Matter*, 2015, **11**, 2993–3002.

11 Wu W., Luo L., Wang Y., Wu Q., Dai H., Li J., Durkan C., Wang N. and Wang G., Endogenous pH-responsive Nanoparticles with Programmable Size Changes for Targeted Tumor Therapy and Imaging Applications, *Theranostics*, 2018, **8**, 3038–3058.

12 Mahmoud A., de Jongh P., Briere S., Chen M., Nowell C., Johnston A., Davis T., Haddleton D. and Kempe K., Carboxylated Cy5-Labeled Comb Polymers Passively Diffuse the Cell Membrane and Target Mitochondria, *ACS Appl. Mater. Interfaces*, 2019, **11**, 31302–31310.

13 Dougherty C., Vaidyanathan S., Orr B. and Banaszak Holl M., Fluorophore:Dendrimer Ratio Impacts Cellular Uptake and Intracellular Fluorescence Lifetime, *Bioconjugate Chem.*, 2015, **26**, 304–315.

14 Simpson J., Ediriweera G., Howard C., Fletcher N., Bell C. and Thurecht K., Polymer Design and Component Selection Contribute to Uptake, Distribution & Trafficking Behaviours of Polyethylene Glycol Hyperbranched Polymers in Live MDA-MB-468 Breast

Cancer Cells, *Biomater. Sci.*, 2019, **7**, 4661–4674.

15 Cilliers C., Nessler I., Christodolu N. and Thurber G., Tracking Antibody Distribution with Near-Infrared Fluorescent Dyes: Impact of Dye Structure and Degree of Labeling on Plasma Clearance, *Mol. Pharmaceutics*, 2017, **14**, 1623–1633.

16 Berezin M., Guo K., Akers W., Livingston J., Solomon M., Lee H., Liang K., Agee A. and Achilefu S., Rational Approach to Select Small Peptide Molecular Probes Labeled with Fluorescent Cyanine Dyes for In Vivo Optical Imaging, *Biochemistry*, 2011, **50**, 2691–2700.

17 Etrych T., Janoušková O. and Chytil P., Fluorescence Imaging as a Tool in Preclinical Evaluation of Polymer-Based Nano-DDS Systems Intended for Cancer Treatment, *Pharmaceutics*, 2019, **11**, 471.

18 Qiu T., Clement P .and Haynes C., Linking Nanomaterial Properties to Biological Outcomes: Analytical Chemistry Challenges in Nanotoxicology for the Next Decade, *Chem. Commun. (Cambridge, U. K.)*, 2018, **54**, 12787–12803.

19 Cai K., Wang A., Yin L. and Cheng J., Bio-nano interface: The Impact of Biological Environment on Nanomaterials and their Delivery Properties, *J. Controlled Release*, 2017, **263**, 211–222.

20 Mignani S., Shi X., Rodrigues J., Roy R., Muñoz-Fernández Á., Ceña V. and Majoral J., Dendrimers toward Translational Nanotherapeutics: Concise Key Step Analysis, *Bioconjugate Chem.*, 2020, **31**, 2060–2071.

21 Pearce A., Rolfe B., Russell P., Tse B., Whittaker A., Fuchs A. and Thurecht K., Development of a Polymer Theranostic for Prostate Cancer, *Polym. Chem.*, 2014, **5**, 6932–6942.

22 Chen L., Simpson J., Fuchs A., Rolfe B. and Thurecht K., Effects of Surface Charge of Hyperbranched Polymers on Cytotoxicity, Dynamic Cellular Uptake and Localization, Hemotoxicity, and Pharmacokinetics in Mice, *Mol. Pharmaceutics*, 2017, **14**, 4485–4497.

23 Ediriweera G., Simpson J., Fuchs A., Venkatachalam T., Van De Walle M., Howard C., Mahler S., Blinco J., Fletcher N., Houston Z., Bell C. and Thurecht K., Targeted and Modular Architectural Polymers Employing Bioorthogonal Chemistry for Quantitative Therapeutic Delivery, *Chem. Sci.*, 2020, **11**, 3268–3280.

24 Chen L., Glass J., De Rose R., Sperling C., Kent S., Houston Z., N. Fletcher, Rolfe B. and Thurecht K., Influence of Charge on Hemocompatibility and Immunoreactivity of Polymeric Nanoparticles, *ACS Appl. Bio Mater.*, 2018, **1**, 756–767.

25 Wang F., Hu K.and Cheng Y., Structure-Activity Relationship of Dendrimers Engineered with Twenty Common Amino Acids in Gene Delivery, *Acta Biomater.*, 2016, **29**, 94–102.

26 Monteiro P., Gulfam M., Monteiro C., Travanut A., Abelha T., Pearce A., Jerôme C., Grabowska A., Clarke P., Collins H., Heery D., Gershkovich P. and Alexander C., Synthesis of Micellar-Like Terpolymer Nanoparticles with Reductively-Cleavable Cross-Links and Evaluation of Efficacy in 2D and 3D Models of Triple Negative Breast Cancer, *J. Controlled Release*, 2020, **323**, 549–564.

27 van den Brand D., Veelken C., Massuger L. and Brock R., Penetration in 3D Tumor

Spheroids and Explants: Adding a Further Dimension to the Structure-Activity Relationship of Cell-Penetrating Peptides, *Biochim. Biophys. Acta, Biomembr.*, 2018, **1860**, 1342–1349.

28 He M., Guo S. and Li Z., In Situ Characterizing Membrane Lipid Phenotype of Breast Cancer Cells using Mass Spectrometry Profiling, *Sci. Rep.*, 2015, **5**, 11298.

29 Howard C., Fletcher N., Houston Z., Fuchs A., Boase N., Simpson J., Raftery L., Ruder T., Jones M., de Bakker C., Mahler S. and Thurecht K., Overcoming Instability of Antibody-Nanomaterial Conjugates: Next Generation Targeted Nanomedicines Using Bispecific Antibodies, *Adv. Healthcare Mater.*, 2016, **5**, 2055–2068.

30 Fletcher N., Houston Z., Simpson J., Veedu R. and Thurecht K., Designed Multifunctional Polymeric Nanomedicines: Long-Term Biodistribution and Tumour Accumulation of Aptamer-Targeted Nanomaterials, *Chem. Commun. (Cambridge, U. K.)*, 2018, **54**, 11538–11541.

31 Sulheim E., Kim J., van Wamel A., E. Kim, Snipstad S., Vidic I., Grimstad I., Widerøe M., Torp S., Lundgren S., Waxman D. and de Lange Davies C., Multi-Modal Characterization of Vasculature and Nanoparticle Accumulation in Five Tumor Xenograft Models, *J. Controlled Release*, 2018, **279**, 292–305.

32 Miao L., Lin C. and Huang L., Stromal Barriers and Strategies for the Delivery of Nanomedicine to Desmoplastic Tumors, *J. Controlled Release*, 2015, **219**, 192–204.

33 Bergeron A. and Gitschier H., *Corning Appl. Note*, 2016, Co-culturing and Assaying Spheroids in the Corning® Spheroid Microplate, Application Note

Table of Contents Graphic